Dependence of trapped-flux-induced surface resistance of a large-grain Nb superconducting radio-frequency cavity on spatial temperature gradient during cooldown through T_c

Shichun Huang,[1,2,3] Takayuki Kubo,[4,5] and R. L. Geng[3,*]

[1]*Institute of Modern Physics, Chinese Academy of Science, Lanzhou 730000, China*
[2]*University of Chinese Academy of Sciences, Beijing 100049, China*
[3]*Thomas Jefferson National Accelerator Facility, Newport News, Virginia 23606, USA*
[4]*KEK, High Energy Accelerator Research Organization, Tsukuba, Ibaraki 305-0801, Japan*
[5]*SOKENDAI (the Graduate University for Advanced Studies), Hayama, Kanagawa 240-0015, Japan*

(Received 3 June 2016; published 26 August 2016)

Recent studies by Romanenko *et al.* revealed that cooling down a superconducting cavity under a large spatial temperature gradient decreases the amount of trapped flux and leads to reduction of the residual surface resistance. In the present paper, the flux expulsion ratio and the trapped-flux-induced surface resistance of a large-grain cavity cooled down under a spatial temperature gradient up to 80 K/m are studied under various applied magnetic fields from 5 to 20 μT. We show the flux expulsion ratio improves as the spatial temperature gradient increases, independent of the applied magnetic field: our results support and enforce the previous studies. We then analyze all rf measurement results obtained under different applied magnetic fields together by plotting the trapped-flux-induced surface resistance normalized by the applied magnetic field as a function of the spatial temperature gradient. All the data can be fitted by a single curve, which defines an empirical formula for the trapped-flux-induced surface resistance as a function of the spatial temperature gradient and applied magnetic field. The formula can fit not only the present results but also those obtained by Romanenko *et al.* previously. The sensitivity $r_{\rm fl}$ of surface resistance from trapped magnetic flux of fine-grain and large-grain niobium cavities and the origin of dT/ds dependence of $R_{\rm fl}/B_a$ are also discussed.

DOI: 10.1103/PhysRevAccelBeams.19.082001

I. INTRODUCTION

The superconducting radio-frequency (SRF) cavity is one of the core components of the present and the future particle accelerators [1]. One of the parameters that describe the performance of an SRF cavity is the unloaded quality factor, Q_0, which is defined by the ratio of the stored energy to dissipation per rf cycle. The definition of Q_0 is reduced to the simple relation, $Q_0 = G/R_s$, where $G \sim \mathcal{O}(10^2)\ \Omega$ is the so-called geometrical factor, determined by the cavity geometry, and R_s is the microwave surface resistance of the inner surface of the cavity. In order to improve Q_0 for a given cavity design, reducing R_s is essential.

The surface resistance R_s consists of two parts: the Bardeen-Cooper-Schrieffer (BCS) resistance $R_{\rm BCS}$ and the residual surface resistance $R_{\rm res}$ [1,2]. The former comes from microwave absorption by the excited quasiparticles. As the temperature T decreases, the quasiparticles cease to be excited, and $R_{\rm BCS}$ exponentially approaches zero. The latter can be further decomposed into two components: $R_{\rm res} = R_{\rm fl} + R_0$. The first term, $R_{\rm fl}$, is a contribution from the trapped flux when the cavity is cooled crossing T_c with a nonzero ambient magnetic field; the second one, R_0, is other residual resistance contributed by precipitates, subgap etc., which depends on material property and is unchanged by cooldown and independent of trapped flux. $R_{\rm res}$ remains finite even at $T \to 0$ therefore sets the limit in attainable Q_0. Since the recently developed impurity doping process significantly reduced $R_{\rm BCS}$ [3–5], the contribution from $R_{\rm res}$ to R_s has relatively increased. The same will be also true in future SRF technologies utilizing alternative materials with smaller $R_{\rm BCS}$ [6–12]. Reduction of $R_{\rm res}$ is one of the present hot topics among SRF researchers.

Romanenko *et al.* demonstrated cooling down under a large spatial temperature gradient decreases the amount of trapped flux and leads to reduction of $R_{\rm res}$ [13]. After their experiments, a lot of measurements of $B_{\rm SC,eq}/B_{\rm NC,eq}$ as a function of a spatial temperature gradient have been carried out [13,14], where $B_{\rm NC,eq}$ and $B_{\rm SC,eq}$ are measured flux densities at the outside of the equator when the cavity is in the normal conducting (NC) and the superconducting (SC) states, respectively. When flux is expelled due to the SC transition, the flux density at the outside of the cavity

*geng@jlab.org

increases or $B_{\mathrm{SC,eq}}$ becomes larger than $B_{\mathrm{NC,eq}}$: a large $B_{\mathrm{SC,eq}}/B_{\mathrm{NC,eq}}$ corresponds to a large ratio of expelled flux. These experiments have repeatedly confirmed the fact that a large spatial temperature gradient improves the ratio of flux expulsion.

While a measurement of $B_{\mathrm{SC,eq}}/B_{\mathrm{NC,eq}}$ is a convenient way to see flux expulsion ratio, an accurate relation between $B_{\mathrm{SC,eq}}/B_{\mathrm{NC,eq}}$ and R_{fl} is not known at present. The direct measurement of R_{fl} is the only way for seeing an effect of spatial temperature gradient on R_{fl}. Nevertheless, only a limited number of systematic studies of R_{res} under a spatial temperature gradient has been reported so far [13,15], where R_{res} does not necessarily equal to R_{fl}. We need to accumulate further experimental data obtained under various spatial temperature gradients and applied magnetic fields. Quantitative studies of the flux expulsion facilitated by a spatial temperature gradient allow one to judge the existing model [16] and other models that may be proposed in the future.

In the present paper, we study the flux expulsion ratio and R_{fl} as functions of the spatial temperature gradient during cooldown under various applied magnetic fields. Our experiment supports the previous observation [13,14] that the flux expulsion ratio improves as the spatial temperature gradient increases, where we use a newly introduced method to evaluate spatial temperature gradients. We adopted the technique used in Ref. [17] for experimental determination of the expulsion ratio. This technique eliminates any cavity geometry, sensor dimension, sensor-cavity misalignment, or cavity flange material dependence in determination of the expulsion ratio. Then we analyze data obtained under different spatial temperature gradient and applied magnetic fields together in one figure and propose an empirical form of R_{fl} as a function of the spatial temperature gradient and the applied magnetic field. The proposed functional form of R_{fl} fits not only data of our experiment but also that of the previous experiment [13]. The sensitivity r_{fl} of surface resistance from trapped magnetic flux of cavities made of fine-grain and large-grain niobium and the origin of dT/ds dependence of R_{fl}/B_a are also discussed.

II. EXPERIMENTS

We measured Q_0, E_{acc} and the magnetic flux density at the cavity outer surface with a controlled applied magnetic field and a varied spatial temperature gradient during a cooldown process. The measurements were carried out by using the dewar 7 and 8 in Jefferson Laboratory vertical test area, where the background magnetic flux density near a single-cell cavity is less than $\sim 0.2\ \mu$T through a combined passive and active compensation shielding.

In the present experiment, we used a single cell cavity named PJ1-2, which is a 1.5 GHz CEBAF upgrade end-cell shape cavity ($G = 285\ \Omega$) made of a high-purity large-grain Nb material supplied from Ningxia Orient Tantalum Industry as shown in Fig. 1(a) [18]. Note that the large-grain niobium disks for the fabrication of this cavity were prepared by using the conventional saw-cutting technique. The disks were further machined in order to reduce the surface roughness. The surface processing of this cavity consists of 90 μm removal by a buffered chemical polishing (BCP) with $\mathrm{HF{:}HNO_3{:}H_3PO_4} = 1{:}1{:}1$ at the room temperature, vacuum furnace outgassing at 800 °C for 3 h, additional 60 μm removal by a BCP with $\mathrm{HF{:}HNO_3{:}H_3PO_4} = 1{:}1{:}2$ at temperature between 8 °C–10 °C, *in situ* baking at 120 °C for 12 h, 30 μm removal by an electropolishing (EP), and another *in situ* baking at 120°C for 12 h.

The setup of the present experiment is schematically shown in Figs. 1(b) and 1(c). Two Cernox thin film resistance temperature sensors, CX-1010-SD-1.4L, named $\mathrm{T_A}$ and $\mathrm{T_B}$ and five silicon diode sensors, XDT-670A-DI-184, named $\mathrm{T_1}$–$\mathrm{T_5}$ were used to monitor the outer surface temperature of the cavity at four different levels: $\mathrm{T_A}$ and $\mathrm{T_B}$ were located at the lower and upper flange, respectively; $\mathrm{T_1}$, $\mathrm{T_2}$ and $\mathrm{T_3}$ were attached to the equator; $\mathrm{T_4}$ was at the top iris; $\mathrm{T_5}$ was at the bottom flange with the same height as $\mathrm{T_A}$. To detect magnetic flux density around the cavity during cooldown processes, three Bartington single-axis magnetic sensors, Mag-01H, named $\mathrm{B_A}$, $\mathrm{B_B}$, and $\mathrm{B_C}$ were used: $\mathrm{B_A}$ and $\mathrm{B_B}$ were paralleled to the cavity axis and set on the equator separated by 90°; $\mathrm{B_C}$ was also paralleled to the cavity axis and set at the top iris. Note that each magnetic sensor at the equator and the top iris is

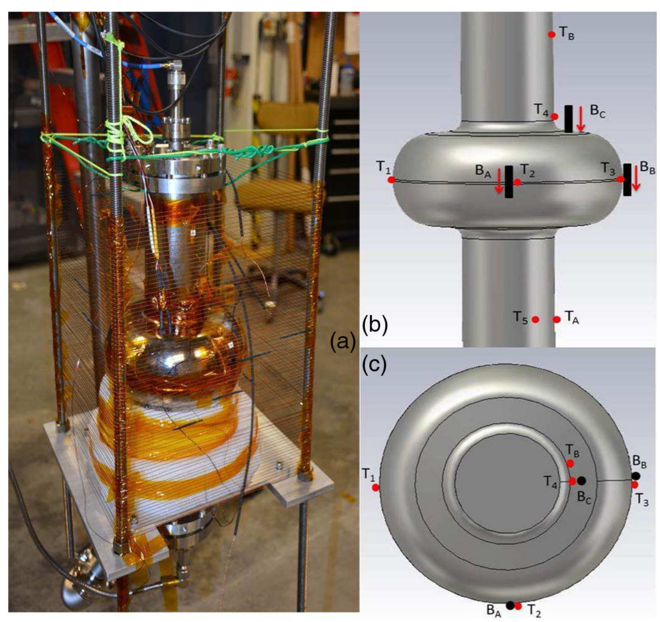

FIG. 1. Experimental setup: A 1.5 GHz single cell cavity located on test stand (a), its front view (b), and top view (c). Red filled circles and black rectangular symbols represent temperature sensors and magnetometers, respectively.

accompanied by a silicon diode temperature sensor to monitor the NC-SC transition at that place. Applied fields parallel to the cavity axis were controlled by rectangle coils wrapping cavity support stainless-steel rods as shown in Fig. 1(a). The beam tube ports of the cavity were capped with stainless-steel plates, indium sealed two cavity flanges.

The procedure is as follows: (1) Measure the generated magnetic field as a function of a coil current at room temperature. (2) Turn off the coil current and cool down the cavity from room temperature to 1.4 K under a tiny background field $< 0.23\ \mu$T (zero-field cooling). (3) Measure Q_0 and E_{acc} at 1.4 K. (4) Measure the magnetic field, $B^{(0)}_{\mathrm{SC,eq}} \equiv (B_A + B_B)/2$, as a function of a coil current at 1.4 K, which approximately corresponds to that for the ideal Meissner state without any trapped flux. (5) Warm up the cavity to a temperature above the critical temperature $T_c = 9.25$ K and set the applied magnetic field B_a by using a coil current recorded in step 1. The accuracy of this procedure in setting B_a is within 1%. The uncertainty mainly comes from the thermal contraction of the setup due to cooldown. (6) Cool down the cavity under the applied magnetic field B_a, where a cooling rate is controlled by adjusting a flow of liquid helium. (7) Measure Q_0 and E_{acc} at 1.4 K again. (8) Measure the magnetic flux density at the equator: $B_{\mathrm{SC,eq}} \equiv (B_A + B_B)/2$. (9) Repeat 5–8 under different cooldown conditions. (10) Repeat 1–9 under a different applied magnetic field B_a. Note that temperatures and magnetic flux densities at the outside surface of the cavity were recorded during all the cooldown and warm-up processes. We named the test with rf measurement as RF2.1 (cool down without the applied field), RF2.2 (cool down with the applied magnetic field) etc.

Some of the tests were conducted without rf testing (i.e. step 3 and 7). These tests focused on the measurement of expelled magnetic flux density under various applied magnetic fields and spatial temperature gradients. We named these sets of measurements Mag2.6, Mag2.7, etc.

It should be noted that, in our experiments, the cavity was electrically isolated from its supporting fixtures. The thermal current in the loop formed by the cavity, test stand top plate, and rf cables were checked by attaching a magnetometer to one of the two rf cables. This sensor was orientated perpendicular to the cable for the maximum sensitivity. The result shows that the thermal current induced magnetic flux density near the cavity iris is no more than 5 nT during the process of cavity cooling through T_c. We believe the thermal current effect [19] can be excluded in our experiments.

III. RESULTS

Figure 2 shows examples of measured temperatures as functions of time. We see the temperatures decrease at each sensor location as time increases and go below T_c during

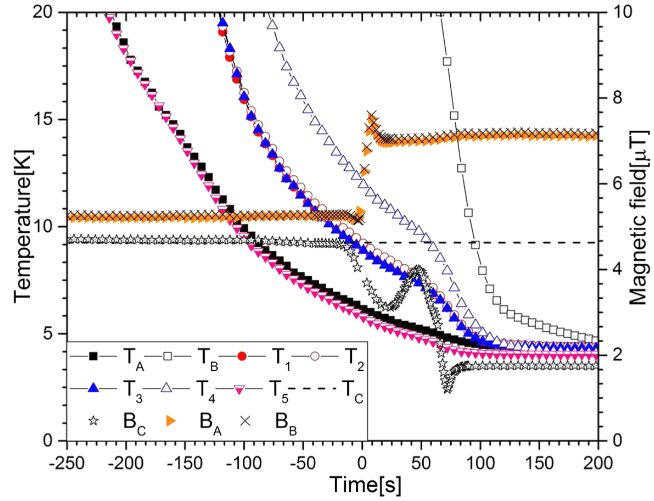

FIG. 2. Examples of measured temperatures and magnetic flux densities as functions of time during a cooldown process, where the applied magnetic field is $\sim 5\mu$T. The horizontal dashed line indicates the critical temperature of Nb, $T_c = 9.25$ K.

$t \simeq \pm 100$ s. For any given cavity location, the cooling rate at the moment of the phase transition, $dT/dt|_{t=t_c}$, can be extracted from the temperature data, where t_c is the time when the sensor at that location showed $T = T_c$. Furthermore, Fig. 3 describes our model of the isothermal front, which is a phase transition front for $T = T_c$, along the path s which follows the curved cavity wall. The temperature gradient is assumed to be zero in the direction normal to s. By using t_c of the sensors placed at different levels, the inverse of the propagation speed of the phase transition front, $v_c^{-1} = dt_c/ds$, can be evaluated, where ds is the line element along the path s. Then the spatial temperature gradient at $t = t_c$ at a sensor location is given by

$$\left.\frac{dT}{ds}\right|_{t_c} = \left.\frac{dT}{dt}\right|_{t_c} \frac{dt_c}{ds}. \tag{1}$$

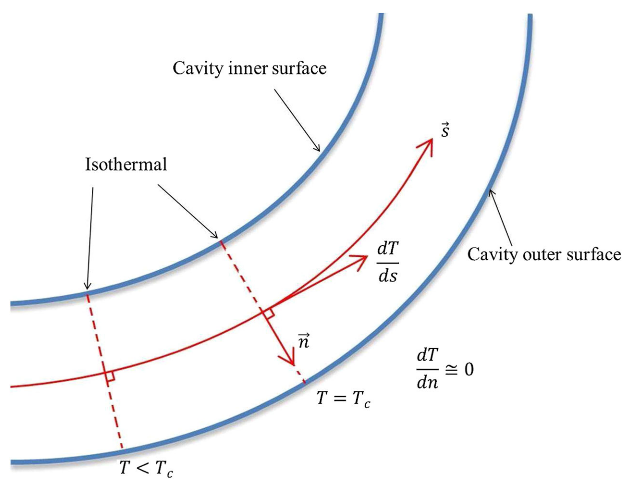

FIG. 3. Model of the temperature gradients at the phase transition front along the curved cavity wall.

TABLE I. Summary of results.

Test	dT/dt (K/sec)	v_c^{-1} (sec/m)	dT/ds (K/m)	$B_{\mathrm{NC,eq}} = B_a (\mu\mathrm{T})$	$B_{\mathrm{SC,eq}}$ (μT)	$B_{\mathrm{SC,eq}}^{(0)}$ (μT)	ϵ_{eq}	R_s (nΩ)	R_{fl} (nΩ)
Mag1.2	0.2010	−7.9	−1.60	5.04	5.15	8.16	0.03	⋯	⋯
RF2.1	⋯	⋯	⋯	⋯	⋯	⋯	⋯	2.33	⋯
RF2.2	0.0082	383.9	3.14	5.19	6.23	8.16	0.35	6.84	5.03
RF2.3	0.0253	127.4	3.23	5.22	5.99	8.16	0.26	8.14	6.33
RF2.4	0.0113	35.4	0.40	5.19	5.80	8.16	0.20	9.6	7.79
RF2.5	0.0425	684.3	29.08	5.25	7.16	8.16	0.65	5.26	3.45
Mag2.6	0.0263	235.6	6.21	5.17	6.23	8.16	0.35	⋯	⋯
Mag2.7	0.0142	38.8	0.55	5.19	5.77	8.16	0.20	⋯	⋯
RF3.1	⋯	⋯	⋯	⋯	⋯	⋯	⋯	2.6	⋯
RF3.2	0.0660	1141.7	75.35	10.25	13.77	14.96	0.75	8.35	5.88
RF3.3	0.2010	−6.9	−1.39	10.02	10.23	14.96	0.04	25	22.53
Mag3.4	0.0262	166	4.34	10.11	11.46	14.96	0.28	⋯	⋯
Mag3.5	0.0035	−682	−2.39	10.12	10.70	14.96	0.12	⋯	⋯
Mag3.6	0.0395	364.5	14.4	10.10	12.68	14.96	0.53	⋯	⋯
Mag3.7	0.0372	352.2	13.09	15.3	18.51	22.70	0.43	⋯	⋯
Mag3.8	0.0852	192.6	16.41	15.31	18.92	22.70	0.49	⋯	⋯
Mag3.9	0.0563	244.9	13.79	15.30	18.82	22.70	0.48	⋯	⋯
Mag3.10	0.0668	749	50.06	15.28	20.38	22.70	0.67	⋯	⋯
Mag3.11	0.0153	202.4	3.10	20.47	22.40	30.44	0.19	⋯	⋯
Mag3.12	0.0592	126.5	7.49	20.48	23.22	30.44	0.28	⋯	⋯
RF4.1	⋯	⋯	⋯	⋯	⋯	⋯	⋯	3.57	⋯
RF4.2	0.0293	1276.7	37.45	15.02	19.48	22.27	0.62	12.74	9.38
RF4.3	0.0318	269.6	8.58	15.28	18.57	22.64	0.45	15.7	12.34
RF4.4	0.0377	88.6	3.34	20.09	22.66	29.98	0.26	28.59	25.24
RF4.5	0.0275	169.5	4.66	20.35	22.48	30.36	0.21	33.81	30.46
RF4.6	0.1795	6.7	1.21	20.35	21.20	30.36	0.09	46.15	42.8
Mag4.7	0.0171	−103.1	−1.77	20.33	21.25	30.36	0.09	⋯	⋯
Mag4.8	0.0251	972.4	24.37	20.33	25.65	30.36	0.53	⋯	⋯

The results are summarized in the second, third, and fourth columns of Table I.

Examples of measured magnetic flux densities are also shown in Fig. 2. We see jumps in the measured magnetic flux densities at the equator occurs at $t = t_c$, which shows the magnetic flux expulsion due to the phase transition from NC state to SC state at that location. A value before the jump, $B_{\mathrm{NC,eq}}$, corresponds to the applied magnetic field B_a, and that after the jump corresponds to $B_{\mathrm{SC,eq}}$. A parameter that represents the magnetic flux expulsion ratio at the equator of the cavity can be defined by

$$\epsilon_{\mathrm{eq}} = \frac{B_{\mathrm{SC,eq}} - B_{\mathrm{NC,eq}}}{B_{\mathrm{SC,eq}}^{(0)} - B_{\mathrm{NC,eq}}} = \frac{\frac{B_{\mathrm{SC,eq}}}{B_{\mathrm{NC,eq}}} - 1}{\frac{B_{\mathrm{SC,eq}}^{(0)}}{B_{\mathrm{NC,eq}}} - 1}, \tag{2}$$

where the denominator corresponds to the increase of magnetic flux density for the ideal expulsion of an applied magnetic field, and the numerator is the increase of magnetic flux density when the cavity is cooled down with the same applied magnetic field. The drop of the magnetic flux density at the iris is also seen, which is a reasonable behavior of the magnetic flux density near a perfect diamagnetic concave (see Ref. [20] for example). The summary of the measured magnetic flux densities is given in the fifth to eighth columns of Table I.

The quantity directly related to the cavity performance is R_s, which can be calculated by using the results of Q_0 and E_{acc} measurements. In the present study, we define R_s at $T = 1.4$ K and $E_{\mathrm{acc}} = 5$ MV/m:

$$R_s \equiv R_s|_{1.4\,\mathrm{K},5\,\mathrm{MV/m}} = \frac{G}{Q_0}\bigg|_{1.4\,\mathrm{K},5\,\mathrm{MV/m}}, \tag{3}$$

where $G = 285\ \Omega$ for our cavity. Values of R_s are summarized in the ninth column of Table I.

The contribution from trapped flux, R_{fl}, can also be extracted from the measurement results. Let us remind the surface resistance is decomposed as $R_s = R_{\mathrm{BCS}} + R_{\mathrm{fl}}(B_{\mathrm{trap}}) + R_0$, where we emphasized that R_{fl} is a function of a trapped flux density at the inner surface of the cavity B_{trap}. Then R_s obtained under the zero-field cooling, where the background field $\lesssim 0.2\ \mu$T, is written as $R_s^{(0)} = R_{\mathrm{BCS}} + R_{\mathrm{fl}}(B_{\mathrm{trap}}^{(0)}) + R_0$, where the index (0) represents the zero-field cooling. Note that R_{BCS} and R_0 are common between R_s and $R_s^{(0)}$, because the surface of the cavity is unchanged during the experiment. Then we find $R_s - R_s^{(0)} = R_{\mathrm{fl}}(B_{\mathrm{trap}}) - R_{\mathrm{fl}}(B_{\mathrm{trap}}^{(0)})$ or

$$R_{\mathrm{fl}} = R_s - R_s^{(0)} + B_{\mathrm{trap}}^{(0)} r_{\mathrm{fl}}, \tag{4}$$

where r_{fl} is the sensitivity defined by $r_{\mathrm{fl}} \equiv R_{\mathrm{fl}}/B_{\mathrm{trap}}$. The first and second terms are given by Eq. (3), and the third term is evaluated in the following paragraph.

Let us evaluate r_{fl}. When B_{trap} is large enough and a resultant R_{fl} is much larger than $R_{\mathrm{BCS}}(1.4\ \mathrm{K})$, we may write $R_s = R_{\mathrm{fl}} + R_0$ and $r_{\mathrm{fl}} = (R_s - R_0)/B_{\mathrm{trap}}$. Furthermore, when almost all of the field is trapped and $B_{\mathrm{trap}} \simeq B_a$, we may write $r_{\mathrm{fl}} = (R_s - R_0)/B_a$. This simplified formula can be applied to the result of RF3.3, where $\epsilon_{\mathrm{eq}} = 0.04$ is so small that we may regard $B_{\mathrm{trap}} \simeq B_a$, and furthermore, $B_{\mathrm{trap}} \simeq B_a = 10\ \mu\mathrm{T}$ and the resultant $R_s = 25\ \mathrm{n}\Omega$ are so large that the contribution from $R_{\mathrm{BCS}}(1.4\ \mathrm{K})$ is negligible. Then we obtain $r_{\mathrm{fl}} = (25\ \mathrm{n}\Omega - R_0)/10\ \mu\mathrm{T}$. To evaluate the unknown constant R_0, we substitute r_{fl} into $R_s^{(0)} = R_{\mathrm{BCS}} + R_0 + r_{\mathrm{fl}} B_{\mathrm{trap}}^{(0)}$, and we find $R_0 = 2.6\ \mathrm{n}\Omega - R_{\mathrm{BCS}} - (25\ \mathrm{n}\Omega - R_0)(B_{\mathrm{trap}}^{(0)}/10\ \mu\mathrm{T})$ or

$$R_0 = \frac{2.6\ \mathrm{n}\Omega - R_{\mathrm{BCS}}(1.4\ \mathrm{K}) - 2.5\ \mathrm{n}\Omega/\mu\mathrm{T} \times B_{\mathrm{trap}}^{(0)}}{1 - \frac{B_{\mathrm{trap}}^{(0)}}{10\ \mu\mathrm{T}}}. \tag{5}$$

Using Eq. (5), we obtain

$$r_{\mathrm{fl}} = \frac{22.4\ \mathrm{n}\Omega + R_{\mathrm{BCS}}(1.4\ \mathrm{K})}{10\ \mu\mathrm{T} - B_{\mathrm{trap}}^{(0)}} \simeq 2.24\ \mathrm{n}\Omega/\mu\mathrm{T}, \tag{6}$$

where $R_{\mathrm{BCS}}(1.4\ \mathrm{K}) \ll 22.4\ \mathrm{n}\Omega$ and $B_{\mathrm{trap}}^{(0)} \ll 10\ \mu\mathrm{T}$ are used.

When all the background magnetic field is assumed to be trapped during the zero-field cooling, $B_{\mathrm{trap}}^{(0)}$ approximately equals to 0.23 μT, 0.06 μT, and -0.1 μT for the measurement of RF2.1, RF3.1 and RF4.1, respectively. Then the third term in Eq. (4) is given by $R_{\mathrm{fl}}(B_{\mathrm{trap}}^{(0)}) = B_{\mathrm{trap}}^{(0)} r_{\mathrm{fl}} \simeq$ 0.52 nΩ, 0.13 nΩ, and 0.22 nΩ for the corresponding $B_{\mathrm{trap}}^{(0)}$. Values of R_{fl} evaluated by using Eq. (4) are summarized in the tenth column of Table I. It should be noted that approximate values of R_0 can be obtained by subtracting the values in the tenth column from those in the ninth column and are given by $R_0 \simeq 2\ \mathrm{n}\Omega$–$3\ \mathrm{n}\Omega$, which are consistent with those evaluated by using $r_{\mathrm{fl}} = (25\,\mathrm{n}\Omega - R_0)/10\mu\mathrm{T}$ or $R_0 = 25\ \mathrm{n}\Omega - 10\ \mu\mathrm{T} \times r_{\mathrm{fl}} \simeq 2.6\ \mathrm{n}\Omega$.

IV. DISCUSSION

A. Dependence of R_{fl}/B_a on dT/ds

Figure 4 shows ϵ_{eq} as functions of dT/dt, dt_c/ds and dT/ds. We emphasize that a rapid cooldown with a large dT/dt does not necessarily lead to a good flux expulsion (e.g. $dT/dt \simeq 0.2\,\mathrm{K/s}$ yields the similar ϵ_{eq} as $dT/dt \simeq 0.02\,\mathrm{K/s}$). The flux expulsion ratio is improved when the spatial temperature gradient, dT/ds, increases. Note that Fig. 4(c) shows ϵ_{eq} as a function of the spatial temperature gradient evaluated by using Eq. (1) and contains results obtained under applied magnetic fields, 5, 10, 15, and 20 μT. A negative dT/ds means that a second phase transition front appeared near the upper iris before the first phase transition front arrived at the upper iris. All these results support and enforce the previous observation that the flux expulsion ratio improves as the spatial temperature gradient increases [13,14].

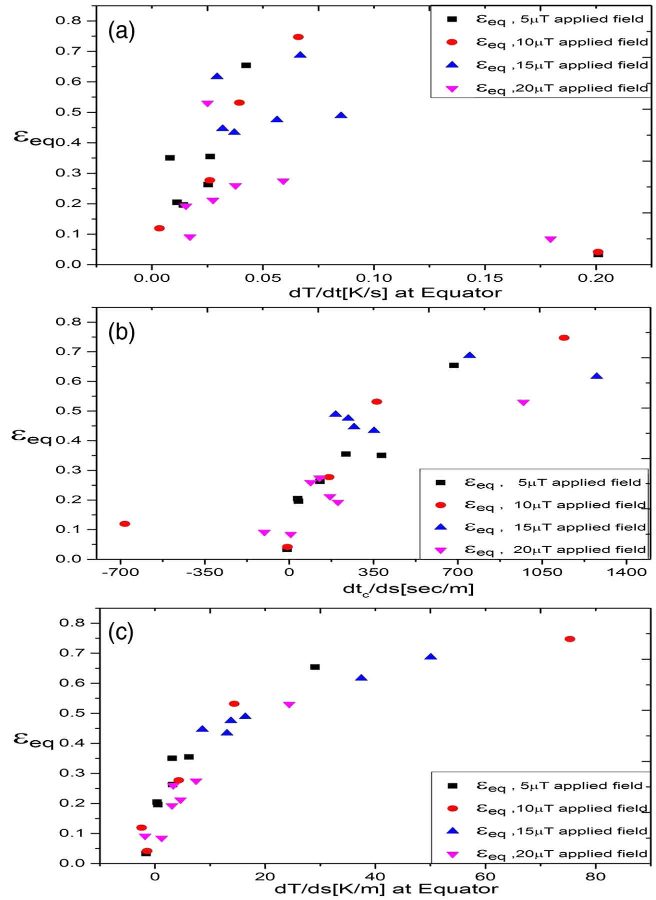

FIG. 4. The flux expulsion ratio ϵ_{eq} as a function of the cooling rate (a), the inverse of the propagation speed of the phase transition front (b) and the temperature gradient (c) when the NC-SC phase transition front arrives at the equator under various applied magnetic fields. The definition of ϵ_{eq} is given by Eq. (2).

Figure 5 shows R_{fl}/B_a as a function of dT/ds. Data points with $dT/ds < 1$ K/m and negative dT/ds are excluded for reasons to be discussed later on. Note here R_{fl}/B_a represents R_{fl} normalized by an applied magnetic field B_a, which allows us to plot all rf measurement results under various applied magnetic fields in one figure. Black squares, red filled circles, blue triangles, and pink upside-down triangles represent results under $B_a = 5$, 10, 15, and 20 μT, respectively. All the plots can be fitted by a single curve,

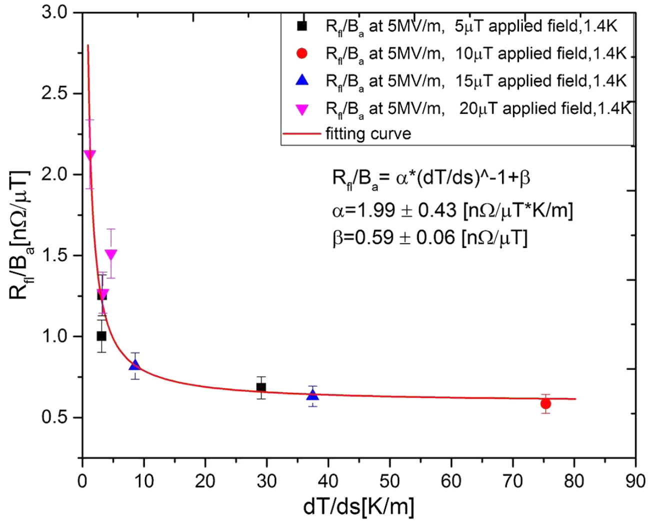

FIG. 5. The $R_{\rm fl}$ normalized by an applied field B_a as a function of dT/ds. The red solid curve represents the fitting curve given by Eq. (7).

$$\frac{R_{\rm fl}}{B_a} = \alpha\left(\frac{dT}{ds}\right)^{-1} + \beta, \tag{7}$$

where $\alpha = 1.99\ {\rm Km^{-1}}\ {\rm n\Omega}/\mu{\rm T}$ and $\beta = 0.59\ {\rm n\Omega}/\mu{\rm T}$. Note that the constants α and β are independent of B_a ($=$ 5, 10, 15, and 20 μT). $R_{\rm fl}$ is always proportional to B_a, decreases with an increase of dT/ds, and approaches βB_a as $dT/ds \to \infty$. The previous study [13] also seems to show the $(dT/ds)^{-1}$ dependence [16], while the constants α and β are different from the present study. Then the $(dT/ds)^{-1}$ dependence may be the general behavior of $R_{\rm fl}$ for an arbitrary cavity, and the constants α and β represent some aspects of material properties of cavity. Experiments with cavities made from different materials or processed by different surface and heat treatments may lead to deeper understanding of physics of the flux expulsion under a spatial temperature gradient. The cavity used in this work is made of large-grain high-purity niobium, final surface processed with EP and low temperature bake, as compared to the cavity used in Ref. [13] which is made of fine-grain high-purity niobium, nitrogen doped and final surface processed by EP. The α value of our cavity is $1.99\ {\rm Km^{-1}}\ {\rm n\Omega}/\mu{\rm T}$, more than 1 order of magnitude smaller than that of Romanenko's cavity, which is $3 \times 10^1\ {\rm Km^{-1}}\ {\rm n\Omega}/\mu{\rm T}$ as shown in Ref. [16].

It should be noted that defining $\tilde{T} = T/T_c$, $\tilde{\alpha} = \alpha/T_c$, and $\tilde{\beta} = \beta T_c/\alpha$, Eq. (7) can be written as $R_{\rm fl} = B_a\tilde{\alpha}[(d\tilde{T}/ds)^{-1} + \tilde{\beta}]$, which is the same form as the formula obtained in Ref. [16]. While Ref. [16] explains the origin of the $(dT/ds)^{-1}$ dependence and naturally introduces $\tilde{\alpha}$ and $\tilde{\beta}$ as material dependent parameters, it does not provide a quantitative framework to evaluate $\tilde{\alpha}$ and $\tilde{\beta}$. A further theoretical work is also expected for understanding the phenomenon, parallel to efforts in experiments.

B. Comparison of sensitivity $r_{\rm fl}$ between large-grain and fine-grain niobium cavities

As the external magnetic field in our study is typically less than 10^2 μT, the trapped fluxoids (or fluxoid bundles) are expected to be well separated and each fluxoid (bundle) in the rf penetration layer individually contributes to rf dissipation. $R_{\rm fl}$ may be written as

$$R_{\rm fl} \propto B_{\rm trap}, \tag{8}$$

where $B_{\rm trap}$ represents the macroscopic trapped flux density on the inner surface of the superconducting cavity. Previously, we have defined the experimentally measurable flux expulsion ratio $\epsilon_{\rm eq}$ in Eq. (2). By argument of symmetry, in the equator region, we may consider the flux expulsion ratio on the inner surface of the cavity is identical to that on the outer surface of the cavity. This leads to the equation for $B_{\rm trap} = (1 - \epsilon_{\rm eq})B_a$ and ultimately

$$R_{\rm fl} = r_{\rm fl}(1 - \epsilon_{\rm eq})B_a. \tag{9}$$

Equation (9) permits one to find the sensitivity $r_{\rm fl}$ for each rf test shown in Table I. The average sensitivity is $\langle r_{\rm fl}\rangle = 1.9\ {\rm n\Omega}/\mu{\rm T}$, consistent within 15% with the value found previously in Eq. (6). This seems to hint that the local flux expulsion ratio elsewhere can be roughly approximated by that at the cavity equator. The 15% variation in $r_{\rm fl}$, which is obtained by averaging the rf losses over the entire inner surface of the cavity, may reflect the nonuniformity in B_a and possible point to point nonuniformity in expulsion ratios.

Now we are ready to compare the $r_{\rm fl}$ measured with our high-purity large-grain niobium cavity with that measured by other workers with high-purity fine-grain niobium cavities at low accelerating field ($E_{\rm acc} \leq 5$ MV/m) (Refs. [21–23]). All cavities have a resonant frequency in the range of 1.3–1.5 GHz. As shown in Fig. 6, $r_{\rm fl}$ of the fine-grain single-cell niobium cavities are in the range of 3–9 ${\rm n\Omega}/\mu{\rm T}$. Note that nitrogen doped cavities made of fine-grain niobium exhibit much larger $r_{\rm fl}$ in the range of 10–50 ${\rm n\Omega}/\mu{\rm T}$ [22], which is not included in Fig. 6. There seems to be a dependence on the surface treatment. For similarly treated surfaces, the $r_{\rm fl}$ of our large-grain niobium cavity is lower by a factor of more than 4 as compared to that of fine-grain niobium cavities. This suggests that the rf dissipation of an elementary fluxoid (or fluxoid bundle) in a large-grain high-purity niobium L-band cavity is intrinsically smaller than in a fine-grain high-purity niobium L-band cavity. It should be mentioned that rf losses due to trapped flux in a large-grain niobium cavity were previously studied in Ref. [24]. A value of sensitivity in the range of 1.4–2.5 ${\rm n\Omega}/\mu{\rm T}$ was reported. Unfortunately,

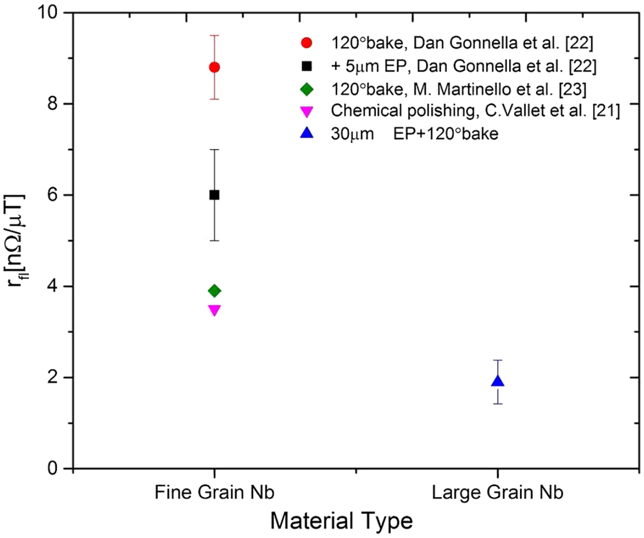

FIG. 6. The sensitivity r_{fl} of cavities made of fine-gain and large-grain niobium with different surface treatments.

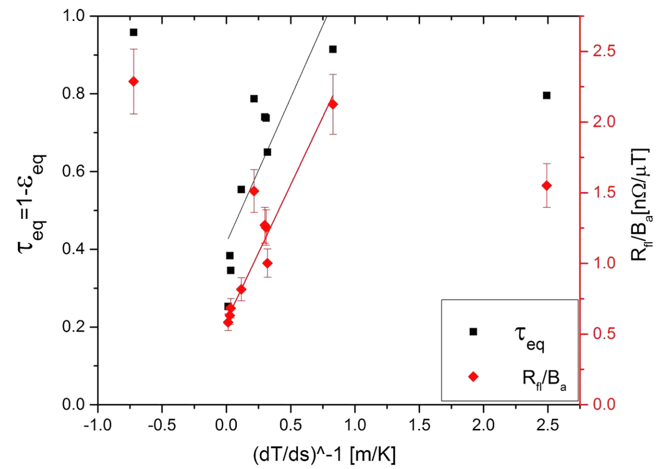

FIG. 7. The magnetic flux trapping ratio $\tau_{\mathrm{eq}}(= 1 - \epsilon_{\mathrm{eq}})$ and R_{fl} normalized by an applied field as functions of the reciprocal of dT/ds for all the data shown in Table I.

no flux expulsion ratio measurement was carried out. Therefore, the sensitivity r_{fl} due to trapped flux as referred to in this paper cannot be derived from Ref. [24].

At a bath temperature of 2 K, 25%–30% higher Q_0 values in nine-cell large-grain high-purity niobium cavities have been previously observed in comparison to nine-cell fine-grain high-purity cavities, both treated by similar electropolishing and low temperature bake and tested in the same testing facilities [25–27]. The ambient magnetic field in these testing facilities is typically shielded or compensated to a value of $< 1.5\ \mu\mathrm{T}$. Data analyses have suggested that these observed higher Q_0 values are due to a lower (by a factor of 2–3) residual surface resistance [25,28]. We now may argue that these observed higher Q_0 (lower residual resistance) in large-grain niobium cavities is a result of the lower r_{fl}, an intrinsic property of the material. Such a property has important implications for practical SRF applications, namely lower rf dissipation can be achieved with a readily available magnetic shielding scheme. This property also tends to drive the optimal operation temperature to < 2 K for the best efficiency of an SRF accelerator.

C. Origin of dT/ds dependence of R_{fl}/B_a

By definition, the sensitivity r_{fl} describes the rf dissipation for a given *trapped* fluxes. Therefore, it is expected to be independent of the process of flux trapping, which occurs during the cooldown of the cavity. If this is true, the dT/ds dependence of R_{fl}/B_a in Eq. (7) is then a shear result of the dT/ds dependence of the flux trapping ratio. As discussed in Sec. IV B, we ignore possible point-to-point variation in the flux expulsion ratio and consider ϵ_{eq} as a rough approximation of the average expulsion ratio. The flux trapping ratio is defined as $\tau_{\mathrm{eq}} = 1 - \epsilon_{\mathrm{eq}}$.

Figure 7 shows τ_{eq} and R_{fl}/B_a as functions of $(dT/ds)^{-1}$ for all the data of ϵ_{eq} and R_{fl}/B_a in Table I. Indeed, the majority of the data points for R_{fl}/B_a and τ_{eq} both follow a rough linear fit. The ratio of the two slopes is 2.29, within 16% of the sensitivity $r_{\mathrm{fl}} = 2.24\ \mathrm{n}\Omega/\mu\mathrm{T}$ found in Eq. (6), which does seem to validate our claim that the dT/ds dependence of R_{fl}/B_a in Eq. (7) is a direct consequence of dT/ds dependence of τ_{eq}. There are two exceptional values in $(dT/ds)^{-1}$ at which both R_{fl}/B_a and τ_{eq} significantly depart from a linear dependence: (1) The first one is a negative dT/ds, which arises from the appearance of a second phase transition front near the upper iris before the arrival of the first phase transition front, originated from the bottom flange. In this case, $\tau_{\mathrm{eq}} \simeq 1$ suggests nearly complete flux trapping. The corresponding R_{fl}/B_a is the largest among all the measured values. This result is compatible with the model of flux confinement by normal conducting islands as proposed in Ref. [29]; (2) The second one is large $(dT/ds)^{-1}$, or small (0.4 K/m) dT/ds. This corresponds to a cool-down scenario with a uniform temperature distribution over the entire length of the cavity. In fact, as realized already in Ref. [16], the linear $(dT/ds)^{-1}$ dependence of R_{fl}/B_a is valid only within an upper and lower limit. The exact values of these limits are not theoretically available yet. Nevertheless, our experimental results seem to indicate that the lower limit is somewhere between 0.4 and 1 K/m. The precision of the present data does not yet allow an experimental determination of the upper limit.

V. SUMMARY

Recent studies [13,14] revealed that cooling down under a large spatial temperature gradient decreases the amount of trapped flux and leads to reduction of R_{fl}.

However, only a limited number of systematic studies of R_{fl} under a spatial temperature gradient have been reported so far [13,15]. There are still many open questions regrading a quantitative understanding to this phenomenon. One of them is the bulk material dependence of this effect.

In the present work, we systematically studied the flux expulsion ratio and R_{fl} of a large-grain high-purity niobium cavity under spatial temperature gradients (0–80 K/m) and various applied magnetic fields (5, 10, 15, and 20 μT). The setup of the experiment is shown in Fig. 1.

As shown in Fig. 4, the flux expulsion ratio improved with an increasing spatial temperature gradient independent of the magnitude of the applied magnetic field, The temperature gradients were calculated by Eq. (1), and the flux expulsion ratio was defined by Eq. (2). These results support and enforce the previous results [13,14].

We plotted all rf measurement results under the applied fields 5–20 μT together in one figure as shown in Fig. 5, where R_{fl} normalized by the applied magnetic field B_a is plotted as a function of the spatial temperature gradient. We found all the data can be fitted by a single curve given by Eq. (7). The constants α and β are independent of B_a, but there is strong material dependence. The α value of our cavity is 1.99 $\mathrm{Km^{-1}\,n\Omega/\mu T}$, more than 1 order of magnitude smaller than that of Romanenko's cavity, which is 3×10^1 $\mathrm{Km^{-1}\,n\Omega/\mu T}$. Equation (7) shows that R_{fl} is always proportional to B_a and decreases down to βB_a with an increasing of the spatial temperature gradient.

We found R_{fl} can be described by Eq. (9), which allows separation of r_{fl}, an intrinsic material dependent parameter, and ϵ_{eq}. We compared the sensitivity r_{fl} of fine-grain and large-grain niobium cavities. The value of r_{fl} of our large-grain niobium cavity is lower by a factor of more than 4 as compared to that of fine-grain niobium cavities final surface treated by the similar procedure of electropolishing and low temperature bake. It suggests that an elementary fluxoid induced rf dissipation in a large-grain high-purity niobium L-band cavity is intrinsically smaller than in a fine-grain high-purity niobium L-band cavity. We now have a better understanding of the previously observed higher Q_0 in large-grain niobium cavities as compared to fine-grain cavities.

The origin of dT/ds dependence of R_{fl}/B_a was also discussed by plotting the magnetic trapping ratio $\tau_{\mathrm{eq}}(= 1 - \epsilon_{\mathrm{eq}})$ and R_{fl}/B_a as functions of $(dT/ds)^{-1}$ in Fig. 7. It does seem to validate our claim that the dT/ds dependence of R_{fl}/B_a in Eq. (7) arises from dT/ds dependence of the flux trapping ratio τ_{eq}. This work may give insights into the mechanism of magnetic flux trapping during the cooldown of SRF cavity into the Meissner state.

A practical consequence of this study is that large-grain high-purity niobium cavities may be intrinsically suitable for reaching higher Q_0, insensitive to cooldown procedure. Therefore it may provide a robust technology for SRF accelerators with improved efficiency.

ACKNOWLEDGMENTS

This work is authored by Jefferson Science Associates, LLC under U.S. DOE Contract No. DE-AC05-06OR23177. Supplemental support is from U.S.-Japan cooperation fund. The work of T. K. is supported by JSPS Grant-in-Aid for Young Scientists (B) 26800157, JSPS Grant-in-Aid for Challenging Exploratory Research 26600142, and Photon and Quantum Basic Research Coordinated Development Program from the Ministry of Education, Culture, Sports, Science and Technology, Japan.

[1] H. Padamsee, J. Knobloch, and T. Hays, *RF Superconductivity for Accelerators* (John Wiley, New York, 1998).

[2] A. Gurevich, Superconducting radio-frequency fundamentals for particle accelerators, Rev. Accel. Sci. Techol. **05**, 119 (2012).

[3] A. Grassellino, A. Romanenko, D. Sergatskov, O. Melnychuk, Y. Trenikhina, A. Crawford, A. Rowe, M. Wong, T. Khabiboulline, and F. Barkov, Nitrogen and argon doping of niobium for superconducting radio frequency cavities: A pathway to highly efficient accelerating structures, Supercond. Sci. Technol. **26**, 102001 (2013).

[4] P. Dhakal, G. Ciovati, and G. R. Myneni, A Path to Higher Q_0 with Large Grain Niobium Cavities, in *Proceedings of the 3rd International Particle Accelerator Conference, New Orleans, Louisiana, USA, 2012* (IEEE, Piscataway, NJ, 2012), p. 2426, WEPPC091.

[5] P. Dhakal, G. Ciovati, G. R. Myneni, K. E. Gray, N. Groll, P. Maheshwari, D. M. McRae, R. Pike, T. Proslier, F. Stevie *et al.*, Effect of high temperature heat treatments on the quality factor of a large-grain superconducting radio-frequency niobium cavity, Phys. Rev. ST Accel. Beams **16**, 042001 (2013).

[6] A. Gurevich, Enhancement of rf breakdown field of superconductors by multilayer coating, Appl. Phys. Lett. **88**, 012511 (2006).

[7] T. Kubo, Y. Iwashita, and T. Saeki, Radio-frequency electromagnetic field and vortex penetration in multilayered superconductors, Appl. Phys. Lett. **104**, 032603 (2014).

[8] A. Gurevich, Maximum screening fields of superconducting multilayer structures, AIP Adv. **5**, 017112 (2015).

[9] S. Posen, M. Liepe, and D. L. Hall, Proof-of-principle demonstration of Nb_3Sn superconducting radiofrequency cavities for high Q_0 applications, Appl. Phys. Lett. **106**, 082601 (2015).

[10] T. Kubo, Field limit and nano-scale surface topography of superconducting radio-frequency cavity made of extreme type II superconductor, Prog. Theor. Exp. Phys. **2015**, 063G01 (2015).

[11] S. Posen, M. K. Transtrum, G. Catelani, M. U. Liepe, and J. P. Sethna, Shielding Superconductors with Thin Films as Applied to rf Cavities for Particle Accelerators, Phys. Rev. Applied **4**, 044019 (2015).

[12] T. Kubo, Theory of Multilayer Coating for Proof-of-Concept Experiments, *Proceedings of SRF2015, Whistler, Canada* (2015), TUBA07.

[13] A. Romanenko, A. Grassellino, A. C. Crawford, D. A. Sergatskov, and O. Melnychuk, Ultra-high quality factors in superconducting niobium cavities in ambient magnetic fields up to 190 mG, Appl. Phys. Lett. **105**, 234103 (2014).

[14] S. Posen, A. Grassellino, A. Romanenko, O. Melnychuk, D. A. Sergatskov, M. Martinello, M. Checchin, and A. C. Crawford, Efficient expulsion of magnetic flux in superconducting rf cavities for high Q_0 applications, arXiv: 1509.03957.

[15] M. Martinello, M. Checchin, A. Grassellino, A. C. Crawford, O. Melnychuk, A. Romanenko, and D. A. Sergatskov, Magnetic flux studies in horizontally cooled elliptical superconducting cavities, J. Appl. Phys. **118**, 044505 (2015).

[16] T. Kubo, Flux trapping in superconducting accelerating cavities during cooling down with a spatial temperature gradient, Prog. Theor. Exp. Phys. **2016**, 053G01 (2016).

[17] C. Benvenuti, S. Calatroni, I. E. Campisi, P. Darriulat, M. A. Peck, R. Russo, and A.-M. Valente, Study of the surface resistance of superconducting niobium films at 1.5 GHz, Physica (Amsterdam) **C316**, 153 (1999).

[18] R. L. Geng *et al.*, New Results of Development on High Efficiency High Gradient Superconducting rf Cavities, in *Proceedings of IPAC2015, Richmond, USA* (2015), p. 3518, WEPWI013.

[19] J.-M. Vogt, O. Kugeler, and J. Knobloch, High-Q_0 operation of superconducting rf cavities: Potential impact of thermocurrents on the rf surface resistance, Phys. Rev. ST Accel. Beams **18**, 042001 (2015).

[20] T. Kubo, Magnetic field enhancement at a pit on the surface of a superconducting accelerating cavity, Prog. Theor. Exp. Phys. **2015**, 073G01 (2015).

[21] C. Vallet *et al.*, Flux Trapping in Superconducting Cavities, in *Proceedings of EPAC1992, Berlin, Germany* (1992), p. 1295.

[22] D. Gonnella, J. Kaufman, and M. Liepe, Impact of nitrogen doping of niobium superconducting cavities on the sensitivity of surface resistance to trapped magnetic flux, J. Appl. Phys. **119**, 073904 (2016).

[23] M. Martinello *et al.*, Trapped Flux Surface Resistance Analysis for Different Surface Treatments, Proceedings of SRF2015, Whistler, Canada (2015), MOPB015.

[24] G. Ciovati and A. Gurevich, Measurement of rf Losses Due to Trapped Flux in a Large-Grain Niobium Cavity, in *Proceedings of SRF2007, Beijing, China* (2007), p. 132, TUP13.

[25] R. L. Geng *et al.*, Q_0 Improvement of Large-Grain Multi-Cell Cavities by Using JLab's Standard ILC EP Processing, in *Proceedings of SRF2011, Chicago, USA* (2011), p. 501, TUPO049.

[26] S. Aderhold, RF Results and Optical Inspection, in *Proceedings of SRF2011, Chicago, USA* (2011), p. 607, WEIOB05.

[27] W. Singer *et al.*, Development of large grain cavities, Phys. Rev. ST Accel. Beams **16**, 012003 (2013).

[28] G. Ciovati, P. Kneisel, and G. Myneini, America's overview of superconducting science and technology of ingot niobium, AIP Conf. Proc. **1352**, 25 (2011).

[29] A. Romanenko, A. Grassellino, O. Melnychuk, and D. A. Sergatskov, Dependence of the residual surface resistance of superconducting radio frequency cavities on the cooling dynamics around T_c, J. Appl. Phys. **115**, 184903 (2014).